UNIVERSITY OF LEEDS

This is a repository copy of *Highly Efficient and Stable CsPbI3 Perovskite Quantum Dots Light-Emitting Diodes Through Synergistic Effect of Halide-Rich Modulation and Lattice Repair*.

White Rose Research Online URL for this paper:
https://eprints.whiterose.ac.uk/222859/

Version: Supplemental Material

Article:
Guo, C., Bi, C., Wei, S. et al. (6 more authors) (2025) Highly Efficient and Stable CsPbI3 Perovskite Quantum Dots Light-Emitting Diodes Through Synergistic Effect of Halide-Rich Modulation and Lattice Repair. Small, 21 (8). 2409630. ISSN 1613-6810

https://doi.org/10.1002/smll.202409630

This is an author produced version of an article published in Small, made available under the terms of the Creative Commons Attribution License (CC-BY), which permits unrestricted use, distribution and reproduction in any medium, provided the original work is properly cited.

Reuse
Items deposited in White Rose Research Online are protected by copyright, with all rights reserved unless indicated otherwise. They may be downloaded and/or printed for private study, or other acts as permitted by national copyright laws. The publisher or other rights holders may allow further reproduction and re-use of the full text version. This is indicated by the licence information on the White Rose Research Online record for the item.

Takedown
If you consider content in White Rose Research Online to be in breach of UK law, please notify us by emailing eprints@whiterose.ac.uk including the URL of the record and the reason for the withdrawal request.

White Rose
university consortium
Universities of Leeds, Sheffield & York

eprints@whiterose.ac.uk
https://eprints.whiterose.ac.uk/

Supporting Information

Highly Efficient and Stable $CsPbI_3$ Perovskite Quantum Dots Light-Emitting Diodes through Synergistic Effect of Halide-rich Modulation and Lattice Repair

Chiyu Guo[†], *Chenghao Bi*[†]*, *Shibo Wei, Ke Ren, Xuexuan Huang, Liang Tao, Xingyu Wang, Nora H. de Leeuw, Wenxin Wang**

C. Guo, C. Bi, S. Wei, K. Ren, X. Huang, L. Tao, W. Wang
College of Physics and Optoelectronic Engineering, Harbin Engineering University, Harbin 150001, China.
Qingdao Innovation and Development Base, Harbin Engineering University, Qingdao 266500, China.

E-mail: chenghao.bi@hrbeu.edu.cn; wenxin.wang@hrbeu.edu.cn.

C. Bi
Yantai Research Institute, Harbin Engineering University, Yantai 264000, P.R. China

X. Wang, N. H. de Leeuw
School of Chemistry, University of Leeds, Leeds LS2 9JT, UK.
Department of Earth Sciences, Utrecht University, 3584 CB Utrecht, The Netherlands.

ORCID
Chenghao Bi: 0000-0002-6074-1412
Manling Sui: 0000-0002-0415-5881
Wenxin Wang: 0000-0001-8191-3976

Experimental Section

Chemicals and Reagents: Cesium carbonate (Cs_2CO_3, Aladdin, 99.9%), lead iodide (PbI_2, Youxuan, 99.9%), lead oxide (PbO, Aladdin, 99.9%), iodotrimethylsilane (TMSI, Aladdin, 97%), guanidinium iodide (GAI, yuriguangneng 99.5%), oleic acid (OA, Alfa-Aesar, 90%), oleylamine (OAm, Aladdin, 90%), 1-octadecene (ODE, Sigma-Aldrich, 90%), n-octane (Aladdin, 98%), methyl acetate (Aladdin, 99%). All these reagents were used without further purification.

Preparation of Cs_2CO_3-OA Precursor

The precursor for synthesizing $CsPbI_3$ QDs is cesium oleate (CsOL). 10 mL of ODE, 1.4 ml of OA, and 204 mg of Cs_2CO_3 were added to 150 mL of the three-neck flask. The mixture was degassed under stirring and then vacuum-stirred at 100°C for 1 hour until Cs_2CO_3 completely dissolved. Nitrogen gas was then introduced into the flask and the system was degassed for 20 min. This process was repeated three times to obtain a cesium-oleate solution that was free from any traces of water and oxygen. The cesium-oleate solution was maintained at approximately 100°C until it was used for QD synthesis.

Preparations of Control-QDs

10 mL of ODE and 173 mg of PbI_2 were mixed in a 150 mL three-neck flask. The mixture was stirred under vacuum conditions at 120°C for 1 hour. Then, 1 mL OA and 1 mL OAm solutions were sequentially added to the mixture. The temperature was raised to 160-165°C under a nitrogen environment. Once all the solutes in the mixture were completely dissolved, 0.8 mL of CsOL solution was injected. The flask was rapidly transferred to an ice-water bath and cooled to room temperature. Then the mixture was transferred to a 100 mL centrifuge tube. 40 mL of methyl acetate was added to the centrifuge tube, followed by centrifugation at a speed of 8000 rpm for 5 min. The precipitate was collected from the centrifuge tube and dispersed in 1 mL of n-octane for use in PeLED fabrication.

Preparations of PbO-OA precursor

10 mL of ODE, 6 mL of OA, and 388 mg of PbO were mixed and added to a 150 mL three-neck flask. The mixture was stirred under vacuum conditions at 100°C for 1 hour, then heated until PbO completely dissolved. Nitrogen gas was put into the flask and the system was degassed for 20 min. This process was repeated three times to obtain a precursor solution that was free from any traces of water and oxygen. The solution was maintained at approximately 100°C until it was used for QD synthesis.

Preparations of I rich-QDs

8 mL of ODE and 1.5 mL of OAm were mixed and added to a 150 mL three-neck flask. The mixture was stirred under vacuum conditions at 100°C for 1 hour. In a nitrogen environment, the temperature was raised to 160-165°C, and then 3.2 mL of lead oleate

precursor solution, 1 mL of CsOL solution, and 0.3 mL of TMSI were added to the mixture. The flask was rapidly transferred to an ice-water bath and cooled to room temperature. The mixture was then transferred to a 100 mL centrifuge tube. 40 mL of methyl acetate was added to the centrifuge tube, followed by centrifugation at a speed of 10,000 rpm for 5 min. The precipitate was collected from the centrifuge tube and dispersed in 2 mL of n-octane for use in PeLED fabrication.

Purification of I rich-QDs and preparations of GAI-QDs

15 mg of GAI powder was accurately weighed and added to the purified I rich-QDs solution. The mixture was stirred at a speed of 3000 rpm for one minute. Afterwards, the solution was transferred to a 5 mL centrifuge tube and centrifuged at 5000 rpm for 5 min. The liquid was collected from the centrifuge tube, resulting in the formation of GAI-QDs.

Characterization of $CsPbI_3$ QDs

Steady-state PL emission was acquired by an F-380 spectrometer. Steady-state ultraviolet-visible (UV-vis) absorption was measured utilizing a Perkin Elmer Lambda 1050+ UV spectrophotometer. An Oxford Instruments Optistat-DN was measured temperature-dependent PL spectra in the range 80-220 K. Transmission electron microscopy (TEM) images were acquired on a JEM-2100 (JEOL) operated at 200 kV. The photoluminescence quantum yields (PLQY) were obtained using an integrating sphere (Edinburgh, FLS920) with an excitation wavelength of 530 nm. The time-resolved photoluminescence decay spectra of QDs were acquired by coupling a Horiba Fluorolog spectrophotometer with a 375 nm, 45ps pulsed laser and a time-corrected single-photon counting system. The TA of the sample was measured using a 1030 nm femtosecond laser as the probing light source, which was generated through an optical parametric amplifier (OPA) to obtain a 420 nm excitation light, through Ultrafast Transient Absorption Spectrometer (TIME-TECH SPECTRA, Co., Ltd. TA-ONE-1). The corresponding transient absorption spectra and the lifetimes of the transient absorption were determined. X-ray diffraction (XRD) was performed using Cu Kα radiation (λ = 1.5418 Å) on an X-ray diffractometer (Bruker, D8 Focus). X-ray photoelectron spectroscopy (XPS) was recorded on a PHI 5000 Versa Probe III spectrometer using a monochromatic AlKα radiation source (1486.6 eV). The time-resolved PL decays (FTIR) of QDs were obtained using a Horiba Fluor log spectrometer with a 375 nm, 45ps pulsed laser and a time-corrected single photon counting system.

Density Functional Theory Calculations

All calculations based on Density Functional Theory (DFT) were performed with the Perdew-Burke-Ernzerhof (PBE) density functional using the generalized gradient approximation (GGA) in the Vienna Ab initio Simulation Package (VASP). Geometry optimizations were carried out for ion-electron interactions using the Projection Augmented Wave (PAW) method. All atomic positions and lattice constants were fully relaxed until the atomic forces were less than 0.02 eV $Å^{-1}$. The total energies of all structures were converged to 10^{-5} eV. A plane-wave cutoff energy of 400 eV was used for the expansion. Electronic structure calculations were performed using an 8 × 8 × 1 Monkhorst-Pack k-point mesh sampling.

Fabrication of PeLEDs devices

ITO-coated glass substrates were cleaned using a sequential process involving detergent, deionized water, ethanol, acetone, and isopropanol, followed by Plasma treatment for 15 min. After UV-ozone treatment, the hole transport layer of PEDOT:PSS was spin-coated at 4000 rpm for 40 s. Subsequently, poly-TPD (8 mg/mL in chlorobenzene) was spin-coated at 2000 rpm for 40 s in a N_2-filled glove box, followed by thermal annealing at 140 ℃ for 15 min. A drop of QDs solution was spin-coated onto the poly-TPD layer at 2000 rpm for 40 s, to fully cover the underneath layer. In a high vacuum (~1×10-5 Pa), TPBi (45 nm), LiF (1 nm), and Al (70 nm) were deposited by thermal evaporation. The active area of the LED was 4 mm^2.

The calculation of the tolerance factor

Generally, for ABX_3 perovskite, the most commonly employed method for comparing structural stability is through the Goldschmidt tolerance factor (t), defined as $t = (r_A + r_X)/\sqrt{2}(r_B + r_X)$[12]. In this formula, r_A represents the ionic radius of the cation, r_B represents the metallic cation, and r_X represents the halide. With ionic radius of 174 pm for Cs, 98 pm for Pb, and 220 pm for I, calculations reveal that the tolerance factor for $CsPbI_3$ is approximately 0.9. Generally, a tolerance factor between 0.8 and 1 indicates an unstable structure that cannot maintain a cubic perovskite configuration at room temperature, leading to the formation of the non-photoactive δ-phase. To address this, proposes a strategy involving the incorporation of GAI to achieve A-site cation substitution. The larger ionic radius of GA^+ compared to Cs^+ effectively increases the tolerance factor. Calculations indicate that the tolerance factor of $GAPbI_3$ can reach approximately 1.5 in extreme cases. Therefore, incorporating a fraction of GA into the material leads to a notable increase in the tolerance factor, significantly enhancing its structural stability.

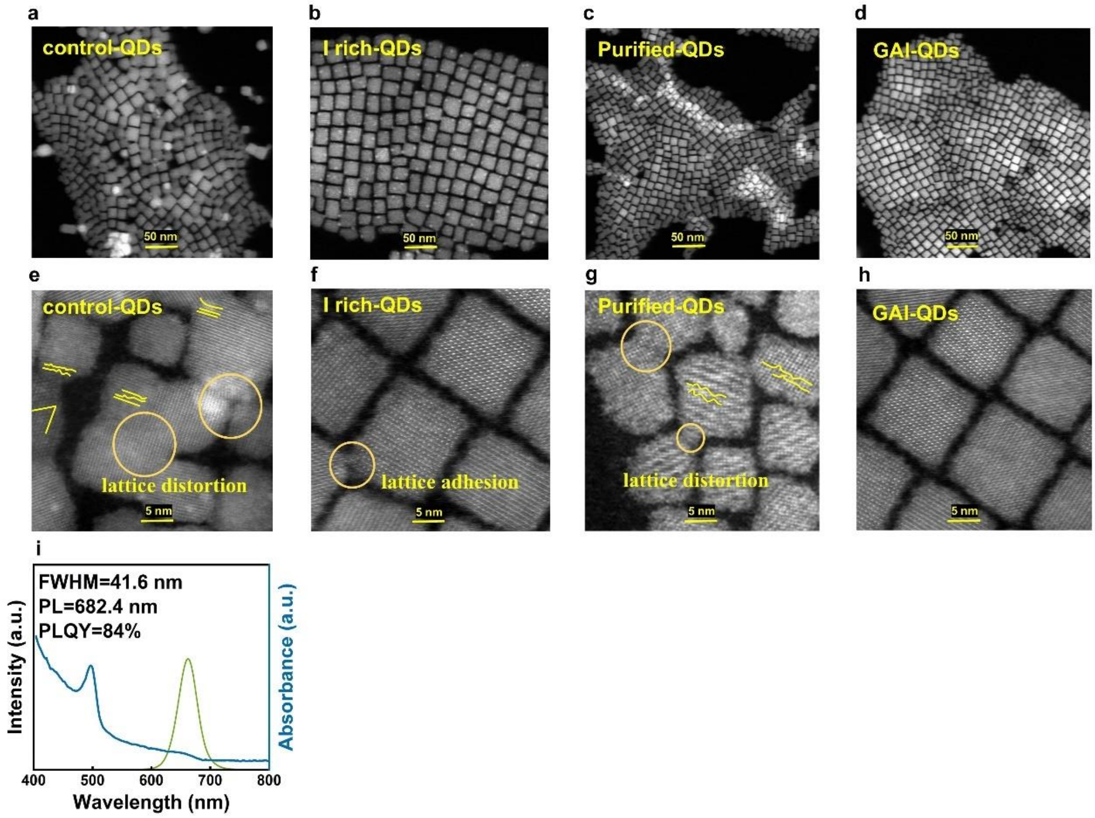

Figure S1. TEM images reflecting the lattice distortion phenomenon: **a)** Control-QDs, **b)** I rich-QDs, **c)** Purified-QDs after purification, **d)** GAI-QDs, magnified images of **e)** Control-QDs, **f)** I rich-QDs, **g)** Purified-QDs, **h)** GAI-QDs. The UV-visible absorption and PL spectra of **i)** Purified-QDs.

Comparison of TEM images for every sample reveals that Control-QDs exhibit severe lattice distortion, while I rich-QDs show minimal lattice adhesion with only minor changes due to ligand detachment. The lattice distortion is highlighted in the figure with yellow lines, lattice adhesion is circled by a reddish-orange circle. I rich-QDs after purification are named as Purified-QDs. It is evident that Purified-QDs exhibit lattice distortion, and their optical properties have significantly degraded. This indicates that the purification process can cause damage to the samples. In contrast, GAI-QDs do not exhibit lattice distortion. This indicates that GAI possesses the ability to repair lattice distortion, significantly enhancing the stability and optical properties of the samples.

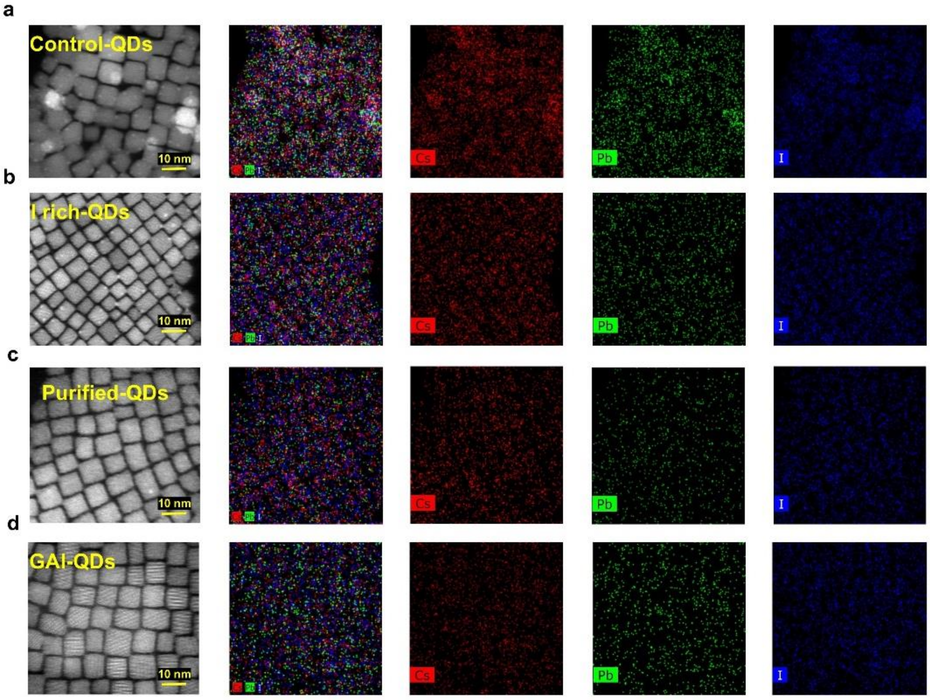

Figure S2. The STEM-HAADF images and EDS mapping of the **a)** Control-QDs (Pb:I = 1.2:2.1), **b)** I rich-QDs (Pb:I = 1.1:3.4), **c)** Purified-QDs (Pb:I =1.2:2.9), **d)** GAI-QDs (Pb:I = 1.1:3.5).

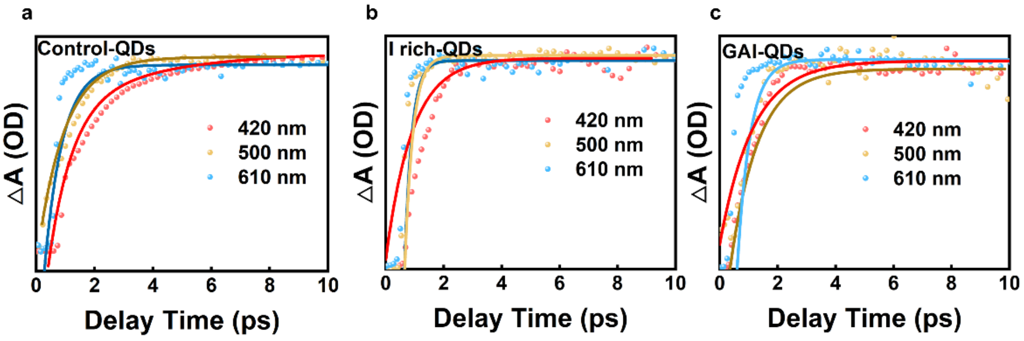

Figure S3. The formation kinetics of the PB band of the **a)** Control-QDs, **b)** I rich-QDs, **c)** GAI-QDs as a function of the excitation wavelength. The excitation energy approaches the bandgap, the ground-state bleach signal appears quickly without a prominent rising component. Excitation energies significantly higher than the bandgap does a distinct rising component appear during the ground-state bleach signal.

As is shown in **Figure S3**, the larger excitation wavelength, the lower corresponding excitation energy. When the excitation energy approaches the bandgap, the ground-state bleach signal appears quickly without a prominent rising component. Only at excitation energies significantly higher than the bandgap does a distinct rising component appear during the ground-state bleach signal, corresponding to the relaxation process of hot charge carriers[1]. Therefore, an excitation wavelength of 420 nm is chosen to investigate the relaxation process.

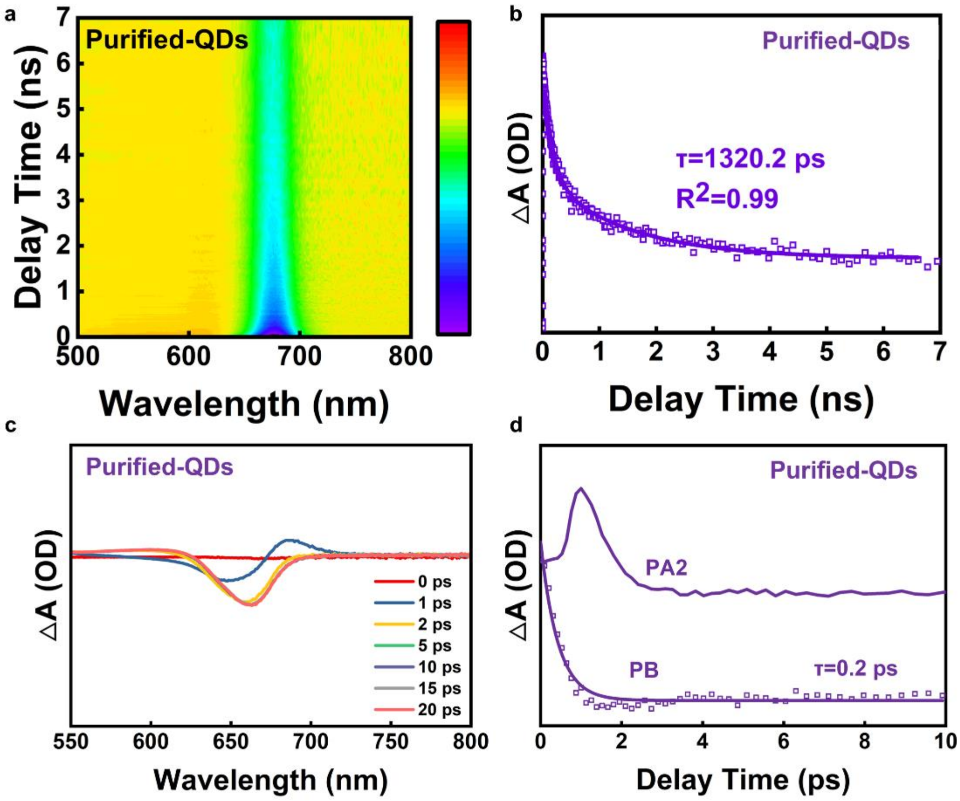

Figure S4. Pseudo color TA plot of **a)** Purified-QDs. **b)** TA bleach recovery curves of Purified-QDs. The TA spectra of **c)** Purified-QDs. **d)** The comparison of the formation and decay kinetics of PB and PA2 bands.

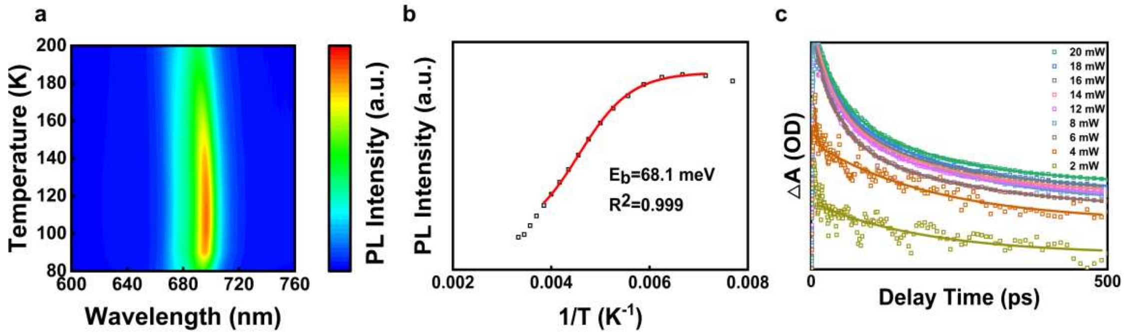

Figure S5. a) Temperature-dependent spectra of Control-QDs, **b)** integrated PL intensity for Control-QDs. **c)** A bleach recovery kinetics of Control-QDs.

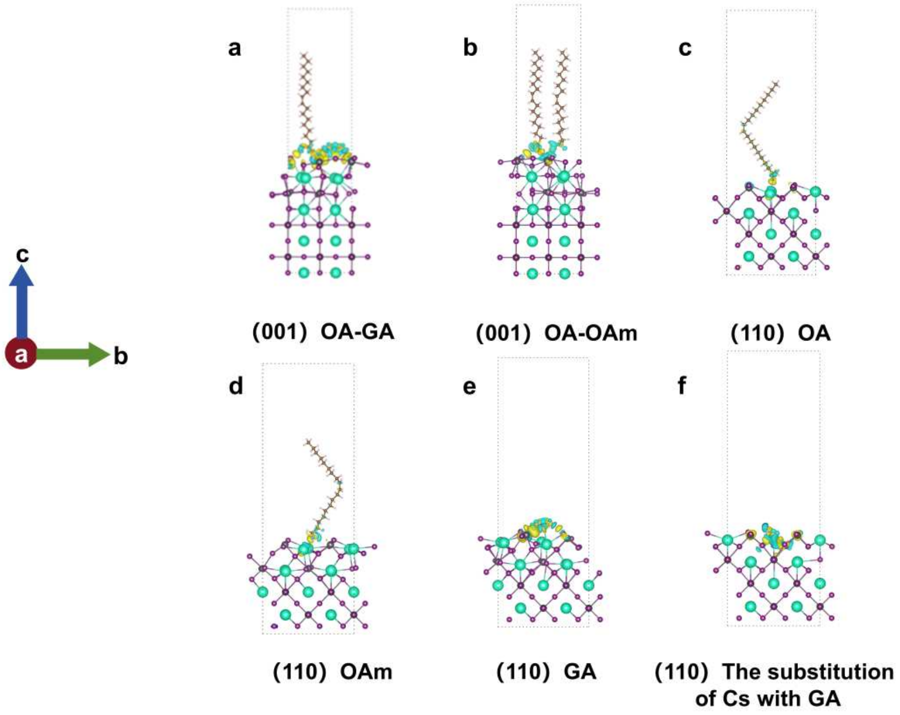

Figure S6. The electronic charge density and distribution of two additional electrons in the vicinity of the valence band (highlighted in yellow) under an external electric field are calculated using Density Functional Theory (DFT) for different ligands. Charge distribution on the (001) surfaces for: **a)** OA-GA ligand, **b)** OA-OAm ligand. Charge distribution on the (110) surfaces for: **c)** OA, **d)** OAm, **e)** GA, **f)** GA ligand replacing a portion of Cs.

Differences in the local charge density resulting from the interaction between OA, OAm, and GA^+ with the QDs surface can be observed in **Figure S6**. The charge transfer between the ligands and QDs demonstrates the strength of the interaction, with blue and yellow regions indicating charge depletion and yellow indicating charge accumulation. On surfaces containing OA and OAm, the charge density is relatively low, while on surfaces containing GA^+, a significant charge concentration around GA^+ can be observed. This phenomenon indicates that GA^+ can be seen as an effective electron acceptor, attracting and aggregating charges around it, significantly reducing carrier clustering and suppressing Auger recombination.

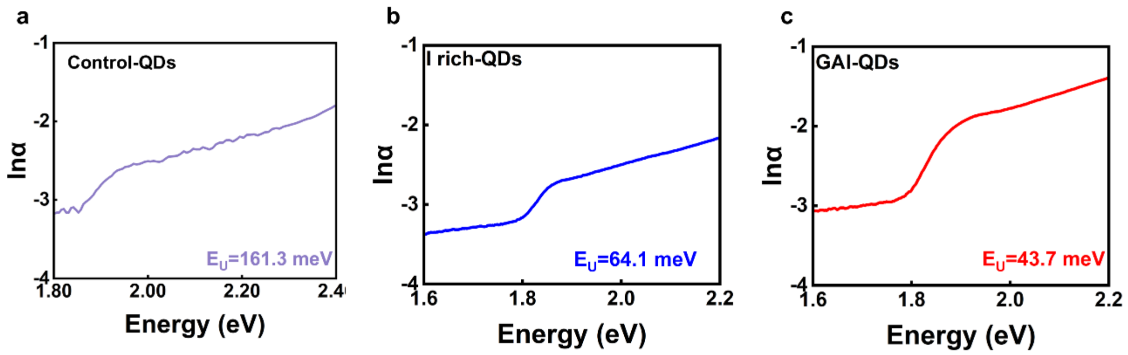

Figure S7. Urbach energies for **a)** Control-QDs, **b)** I rich-QDs, **c)** GAI-QDs.

A comparison of E_u of the three samples reveals that the E_u values for Control-QDs, I rich-QDs, and GAI-QDs are 161.3, 64.1, and 43.7 meV. This indicates that Control-QDs exhibit the highest density of trap states than other QDs at the material surface. This observation further corroborates the improved coordination environment of Pb ions on the surface of GAI-QDs.

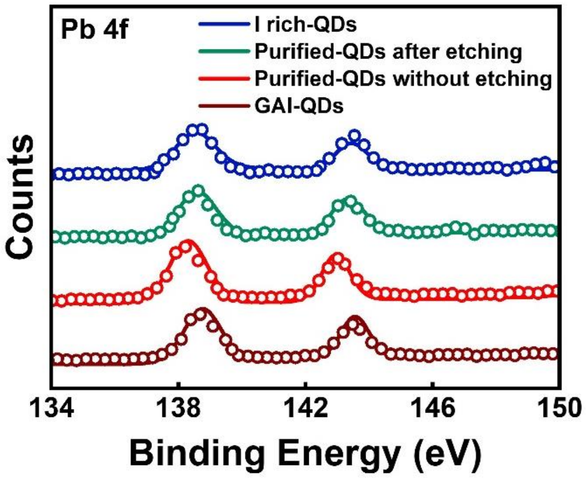

Figure S8. Pb 4f XPS spectra of I rich-QDs, Purified-QDs after Ar ion etching, Purified-QDs without Ar ion etching and GAI-QDs.

Figure S8 presents a comparative XPS analysis of I rich-QDs, and the depth-resolved XPS measurements of Purified-QDs. We can measure the XPS signal of different depth in QDs based on the Ar ion etching. The Purified-QDs without etching show the surface information of Purified QDs and the Purified-QDs after etching show the inner chemical bond information of Purified-QDs. Comparison of the Pb 4f energy levels reveals that the core level peaks of the Purified-QDs with etching are similar with those of the I rich-QDs, both located at 138.1 eV and 143.2 eV. This indicates a low density of vacancy defects and similar coordination environment around the Pb ions in both QDs. However, the Pb 4f core level peaks of the Purified-QDs surface are located at lower binding energies than those of the Purified-QDs inner and the I rich-QDs. This shows a weaker Pb–I interaction in the PbI_6^{4-} octahedra of the Purified-QDs, which is attributed to the increased density of vacancy defects on the QDs surface during the purification. Therefore, we can conclude that the defects in the purified Purified-QDs are primarily located at the surface. The primary purpose of the subsequent GAI treatment is used to repair the surface lattice of the QDs. **Figure S8** clearly shows that after GAI treatment, the Pb 4f energy level peaks of the GAI-QDs shifted to higher binding energies, removing to 138.2 eV and 143.4 eV. This indicates effective repair of surface defects in the QDs via GAI treatment, and a significant improvement in the coordination environment of the Pb ions.

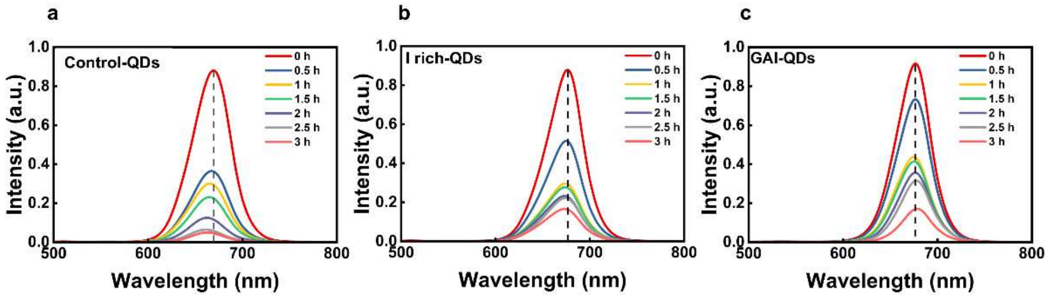

Figure S9. The spectral stability of **a)** Control-QDs, **b)** I rich-QDs, and **c)** GAI-QDs are verified through prolonged UV light irradiation in a dark environment, with testing conducted every 30 min.

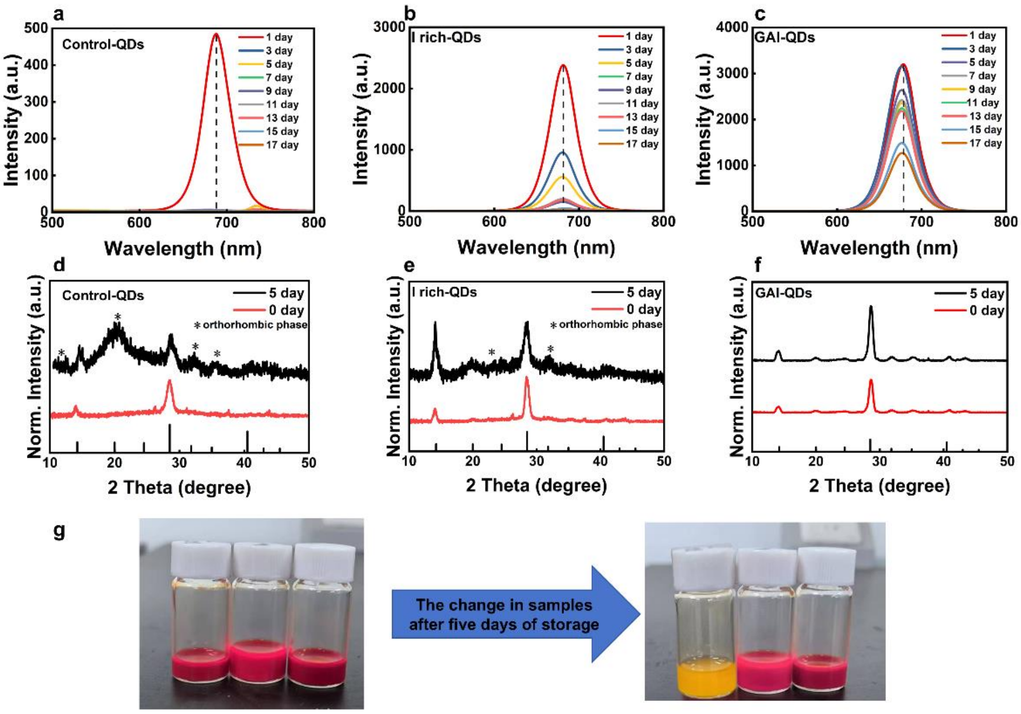

Figure S10. The PL spectrum stability of **a)** Control-QDs, **b)** I rich-QDs, and **c)** GAI-QDs are tested over a period of half a month at room temperature, stored in a dark environment, with testing conducted every two days. XRD comparison of **d)** Control-QDs, **e)** I rich-QDs, and **f)** GAI-QDs before and after storage for five days. **g)** Comparison of the luminescence properties of the three samples before and after storage for five days.

Figure S10 a-c present a comparison of the PL spectrum stability of three samples at room temperature. Control-QDs exhibit the poorest stability. While I rich-QDs demonstrate significantly improved stability, I rich-QDs are still unable to maintain luminescence for more than two weeks. GAI-QDs exhibit the best stability, retaining normal luminescence even after two weeks. As shown in **Figure S9 d-f**, after a period of time, Control-QDs exhibit numerous orthorhombic phase peaks due to phase transformation, while I rich-QDs also show a small number of impurity peaks. In contrast, GAI-QDs do not exhibit any changes. As shown in **Figure S9 g**, from left to right, the three samples are Control-QDs, I rich-QDs, and GAI-QDs. After being stored for five days, the precipitate observed at the bottom of the Control-QDs solution, which turns yellow upon further dissolution in n-octane, indicates that Control-QDs transform to the non-luminescent δ orthorhombic phase. I rich-QDs shows a slight fading in color, while GAI-QDs remains largely unchanged. This demonstrates that GAI-QDs possess the best stability among the three.

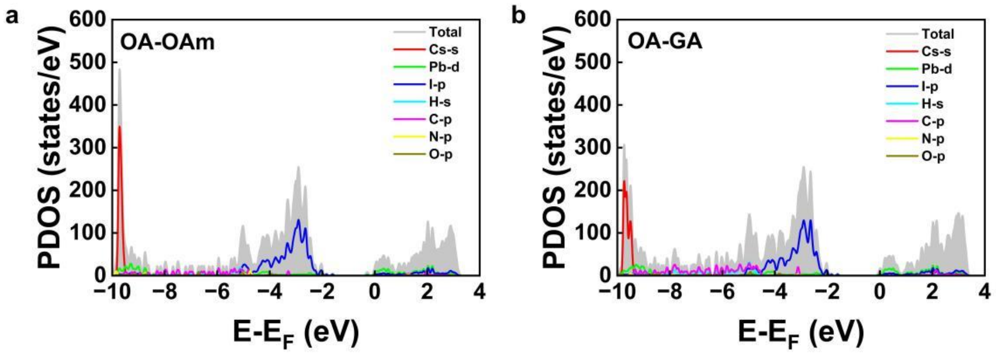

Figure S11. Differential charge density distributions of **a)** OA-OAm, **b)** OA-GA interactions.

In **Figure S11**, the overlap between the Cs, Pb, and I orbitals of the QDs and the C, H, and N orbitals of the organic ligands implies potential orbital hybridization between the ligands and QDs, leading to energy overlap. Conversely, the absence of overlap indicates that the band-edge characteristics are determined solely by the QDs or ligands. Compared to the attachment of OA and OAm ligands, the density of state overlap between GA^+ and the OA ligand and QDs increases in the energy range from -6 to -3 eV. This suggests a stronger interaction between GA^+ and the OA ligand and QDs than between the OA and OAm ligands. Furthermore, these overlap regions between the ligands and QDs are located within the bandgap, indicating that these ligands do not directly affect the optical properties of the QDs but rather influence the optoelectronic properties after surface modification. Based on the theoretical and experimental results, we conclude that replacing OAm with GA^+ can significantly reduce the defect density, improve structural stability, suppress Auger recombination, and greatly enhance the relaxation time.

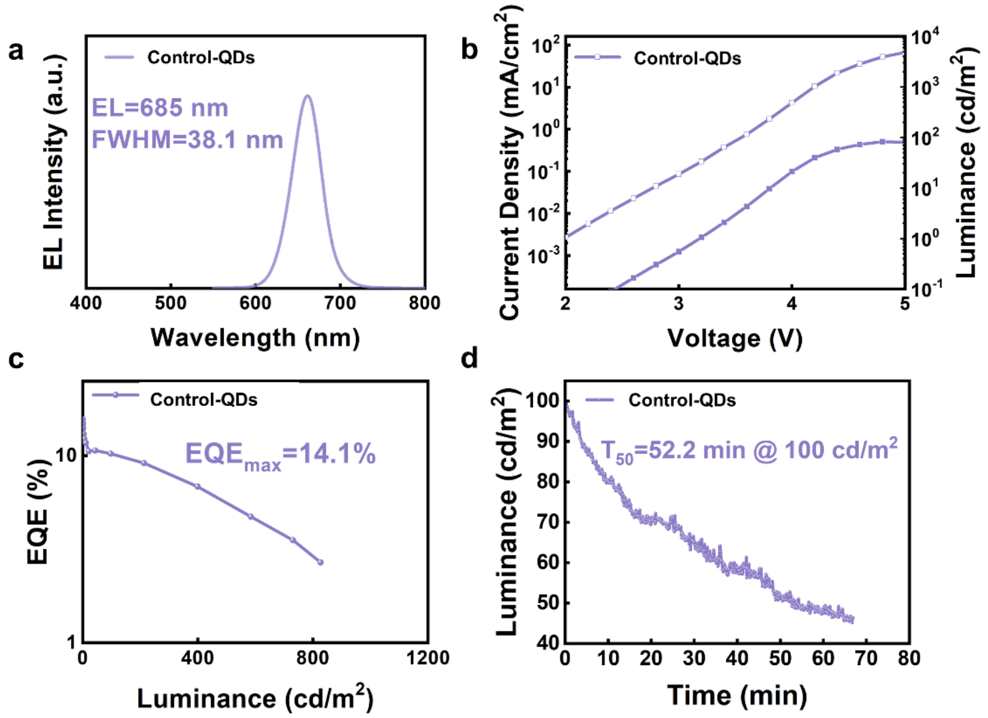

Figure S12. a) EL spectra of PeLEDs based on Control-QDs. **b)** J-V-L curves of PeLEDs based on Control-QDs. **c)** EQE-L curves of PeLEDs based on Control-QDs. **d)** Operational half-lifetime T_{50} of PeLEDs based on Control-QDs at an initial luminance of 100 cd/m^2.

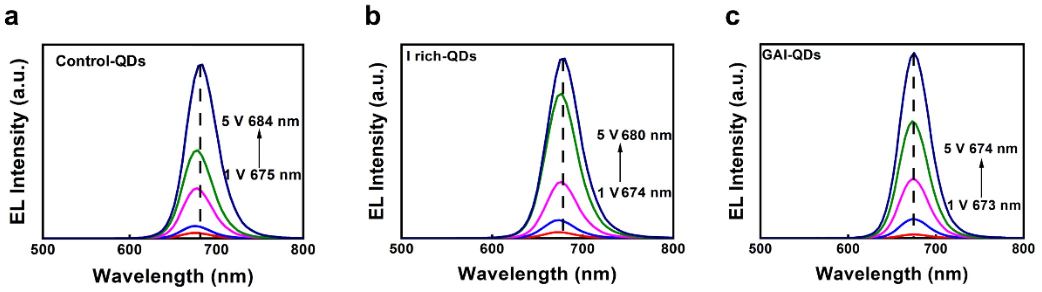

Figure S13. The EL spectra of devices prepared using **a)** Control-QDs, **b)** I rich-QDs, and **c)** GAI-QDs at different operating voltages of 1-5V.

The stability of the EL operating voltages for the three types of QDs is compared (**Figure S13**). It is evident that as the operating voltage increases, GAI-QDs only exhibit a red shift of 1 nm, I rich-QDs show a red shift of 6 nm, and Control-QDs exhibit a red shift of 9 nm. Among them, Control-QDs show the poorest working stability, while GAI-QDs demonstrate the best working stability.

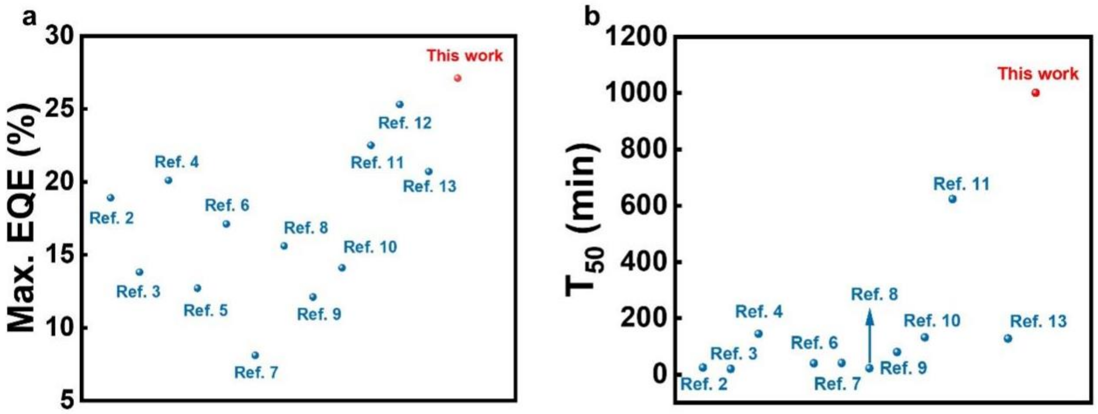

Figure S14. A performance comparison of PeLEDs device with red emission: **a)** EQE, **b)** T_{50}.

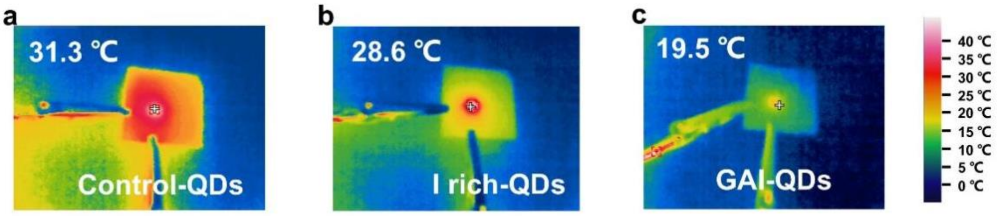

Figure S15. Temperature measurements were taken using an infrared thermal imager after continuous operation for 10 min at room temperature (10 °C) and 5 V applied voltage for **a)** PeLEDs based on Control-QDs, **b)** I rich-QDs, and **c)** GAI-QDs.

Auger recombination proceeds primarily through three pathways: intradot biexciton Auger recombination, trap-assisted Auger recombination and diffusion-assisted Auger recombination[16]. Intradot biexciton Auger recombination occurs when two excitons are generated within a single QDs. One exciton non-radiatively transfers its energy to the remaining carrier, predominantly dissipating this energy as heat. Device heating during operation significantly impacts device stability[16-18].At same or higher brightness, stronger Auger recombination can lead to increased heat accumulation and induce phase transitions in QDs, thereby affecting the performance of PeLEDs. This pathway of Auger recombination therefore impacts device operational stability at high brightness. Trap-assisted Auger recombination involves the trapping of charge carriers at surface defects of the QDs, facilitating energy transfer to another band-edge carrier. This energy transfer process significantly impacts the EQE of PeLEDs. In diffusion-assisted Auger recombination, the charge carrier concentration within the QDs increases via diffusion[19]. Higher charge carrier concentrations and charge-carrier mobility leads to a greater probability of Auger recombination. During PeLEDs operation, the charge carrier mobility increases under the influence of the applied electric field. Electrical excitation itself is a form of high-density excitation, which can lead to the accumulation of carriers, resulting in limited maximum brightness under high current density conditions for the device. Additionally, at high brightness levels, the efficiency drops, causing thermal accumulation that undermines the stability of the device. Consequently, Auger recombination is readily promoted in operating PeLEDs, leading to efficiency roll-off at high brightness. In summary, regardless of the pathway, Auger recombination significantly reduces the EQE, operational stability, and lifetime of the device[20].

As shown in **Figure S15**, operating continuously for 10 min under room temperature and a working voltage of 5 V, the temperature of the PeLEDs based on Control-QDs reach 31.3 °C, the PeLEDs based on I rich-QDs exhibit a slightly lower temperature of 28.6 °C, while the PeLEDs based on GAI-QDs show a lowest temperature of only 19.5 °C. For PeLEDs, the length of the surface ligands on the QDs, defect density, and Auger recombination all contribute to device heating. Compared to PeLEDs based on Control-QDs, the temperature of PeLEDs based on I rich-QDs show a slight decrease, primarily attribute to the reduced defect density in the I rich-QDs. However, this decrease is only 2.5 °C, indicating that a reduction in defect density alone is insufficient to effectively relief PeLEDs heating. Compared to PeLEDs based on I rich-QDs, the temperature of PeLEDs based on GAI-QDs reduce to 19.5 °C. This is mainly because the introduction of GAI in GAI-QDs significantly inhibits phonon coupling compared to I rich-QDs, reducing the thermal loss caused by intradot biexciton Auger recombination. Additionally, GAI passivates surface defects, minimizing the generation of trap-assisted Auger recombination. Comparative analysis clearly demonstrates that Auger recombination exerts a significantly greater influence on the operating temperature of PeLEDs.

Table S1. Concentration of different elements in Control-QDs, I rich-QDs, GAI-QDs calculated from the EDS mapping.

Sample Code	Element	Atomic Fraction (%)	Cs/Pb/I
Control-QDs	Cs	23.3	1:1.2:2.1
	Pb	28.3	
	I	48.4	
I rich-QDs	Cs	18.3	1:1.1:3.4
	Pb	20.1	
	I	61.6	
Purified-QDs	Cs	18.1	1:1.2:2.9
	Pb	21.0	
	I	60.9	
GAI-QDs	Cs	17.8	1:1.1:3.5
	Pb	20.1	
	I	62.1	

Table S2. Summary of TA spectra fitting parameters for Control-QDs, I rich-QDs, Purified-QDs, GAI-QDs.

Sample Code	**f_1 [%]**	**τ_1 [ps]**	**f_2 [%]**	**τ_2 [ps]**	**τ [ps]**
Control-QDs	13.9	83.0	86.1	1148.5	1000.7
I rich-QDs	9.8	95.4	90.2	1558.1	1414.6
Purified-QDs	13.0	160.0	87.0	1493.5	1320.2
GAI-QDs	8.6	167.9	91.4	2777.7	2552.9

As shown in **Table 2**, the ratio of τ_1 of Control-QDs, I rich-QDs, Purified-QDs and GAI-QDs are 13.9%, 9.8%, 13.0% and 8.6%. The τ of Control-QDs, I rich-QDs, Purified-QDs and GAI-QDs are 1000.7 ps, 1414.6 ps, 1320.2 ps and 2552.9 ps. The significantly longest τ of GAI-QDs compared to the other samples suggests that the Auger recombination process is minimal in GAI-QDs, indicating a lower defect density. Control-QDs exhibit the most severe Auger recombination, resulting in the shortest lifetime. The halogen-rich environment employed in the fabrication of I rich-QDs effectively suppressed Auger recombination. However, comparison with Purified-QDs, demonstrates that the purification process introduces amounts of I vacancies, it has a detrimental effect on lifetime and induces more serious Auger recombination. To address this issue, GAI is used to optimize. The resulting GAI-QDs exhibit a significantly longer τ, indicating minimal Auger recombination and a lower defect density.

Table S3. Summary of TA spectra fitting parameters for solutions of I rich-QDs, GAI-QDs under the pulse energy density of 20 mW.

Sample Code	**f_1 [%]**	**t_1 [ps]**	**f_2 [%]**	**t_2 [ps]**
I rich-QDs	24.5	22.8	75.5	158.1
GAI-QDs	6.9	73.4	93.1	557.1

Table S4. Summary of TA spectra fitting parameters for solutions of I rich-QDs, GAI-QDs under the pulse energy density of 4 mW.

Sample Code	f_1 [%]	t_1 [ps]	f_2 [%]	t_2 [ps]
I rich-QDs	100.0	144.0	/	/
GAI-QDs	100.0	192.1	/	/

Further analysis of the changes in bleaching recovery dynamics curves in the two states reveals normalized data for I rich-QDs and GAI-QDs at different power levels, as shown in **Tables S3 and S4**. At a low power of 4 mW, the bleaching recovery dynamics of I rich-QDs and GAI-QDs exhibit single exponential decay. The decay lifetimes for I rich-QDs and GAI-QDs are 143.99 ps and 192.07 ps Relatively, the single exciton fitting lifetime of GAI-QDs has been improved to some extent. At a high power of 20 mW, two lifetime components are observed. The fast decay components for I rich-QDs and GAI-QDs are 22.81 ps (24.5%) and 73.36 ps (6.9%). The slow decay components are 158.06 ps (75.5%) for I rich-QDs and 557.11 ps (93.1%) for GAI-QDs. This indicates that after optimization, the generation of Auger recombination has been greatly suppressed.

Table S5. Summary of TRPL fitting parameters for Control-QDs, I rich-QDs, GAI-QDs. The deviation of $k_{nr} \times 10^{7} s^{-1}$ is calculated when the PL QY uncertainty is +/-0.5% and that of the lifetimes is +/-0.1ns.

Sample Code	**f_1 [%]**	**t_1 [ns]**	**f_2 [%]**	**t_2 [ns]**	**τ [ns]**	**PLQY [%]**	**τ_{nr} [ns]**	**k_{nr} [10^{-13} s^{-1}]**
Control-QDs	78.7	21.3	21.3	42.2	25.8	67.0	78.1	128.1
I rich-QDs	91.0	26.3	9.0	60.0	29.3	84.0	183.0	54.6
GAI-QDs	100.0	70.3	-	-	70.3	97.0	2342.3	4.3

Table S6. Summary of the performance of a typical PeLED device with red emission.

Materials	**EL Peak [nm]**	**Max. Luminance [cd/m^2]**	**Max. EQE [%]**	**Operational lifetime [min]**	**Ref.**
$Cs_{0.9}GA_{0.1}PbI_3$ (QDs)	688	3486	18.9	25	[2]
$CsPbI_3$ (QDs)	695	7039	13.8	20	[3]
E-$CsPbI_3$ (QDs)	650	4932	20.1	145	[4]
$CsPbI_3$ (QDs)	685	6000	12.7	/	[5]
$CsPbI_3$:1.8% Sr^{2+} (NC)	687	586	17.1	40	[6]
$CsPb_{1-X}Zn_xI_3$ (NC)	688	2990	8.1	41	[7]
$CsPbI_3$ (QDs)	686	1643	15.6	22.2	[8]
EC-$CsPbI_3$ (NC)	686	1674	12.1	80	[9]
γ-$CsPbI_3$（film)	700	1325	14.1	132	[10]
$CsPbI_3$ (QDs)	668	955	22.5	624	[11]
γ-$CsPbI_3$ (NC)	687	13626	25.3	/	[12]
$CsPbI_3$ (NC)	681	3861	20.7	128	[13]
GAI-QDs	683	3949	27.1	1001.1	This work

Reference

[1] a)Y. Yang, D. P. Ostrowski, R. M. France, K. Zhu, J. Van De Lagemaat, J. M. Luther, M. C. Beard, *Nat. Photonics* **2016**, 10, 53; b)J. Fu, Q. Xu, G. Han, B. Wu, C. H. A. Huan, M. L. Leek, T. C. Sum, *Nat. Commun.* **2017**, 8, 1300.

[2] P. Serafini, A. Villanueva-Antolí, S. D. Adhikari, S. Masi, R. S. Sánchez, J. Rodriguez-Pereira, B. Pradhan, J. Hofkens, A. F. Gualdrón-Reyes, I. Mora-Sero, *Chem. Mater.* **2023**, 35, 3998.

[3] M. T. Hoang, A. S. Pannu, Y. Yang, S. Madani, P. Shaw, P. Sonar, T. Tesfamichael, H. Wang, *Nano-Micro Lett.* **2022**, 14, 69.

[4] J. Guo, Y. Fu, W. Zheng, M. Xie, Y. Huang, Z. Miao, C. Han, W. Yin, J. Zhang, X. Yang, *Nano Lett.* **2023**, 24, 417.

[5] Y. Wang, Y. Teng, P. Lu, X. Shen, P. Jia, M. Lu, Z. Shi, B. Dong, W. Yu, Y. Zhang, *Adv. Funct. Mater.* **2020**, 30, 1910140.

[6] C. Chen, T. Xuan, W. Bai, T. Zhou, F. Huang, A. Xie, L. Wang, R. Xie, *Nano Energy* **2021**, 85, 106033.

[7] X. Shen, H. Wu, X. Zhang, M. Xu, J. Hu, J. Zhu, B. Dong, W. Yu, X. Bai, *J. Phys. Chem. Lett.* **2020**, 12, 94.

[8] S. Yang, C. Bi, W. Dong, X. Zhang, W. Zheng, W. C. Choy, J. Tian, *Adv. Opt. Mater.* **2022**, 10, 2200189.

[9] S. Sun, P. Jia, M. Lu, P. Lu, Y. Gao, Y. Zhong, C. Tang, Y. Zhang, Z. Wu, J. Zhu, *Adv. Funct. Mater.* **2022**, 32, 2204286.

[10] Q. Zhang, Y. Song, J. Hao, Y. Lan, L. Feng, X. Ru, J. Wang, K. Song, J. Yang, T. Chen, *J. Am. Chem. Soc.* **2022**, 144, 8162.

[11] H. Ebe, R. Suzuki, S. Sumikoshi, M. Uwano, R. Moriyama, D. Yokota, M. Otaki, K. Enomoto, T. Oto, T. Chiba, *Chem. Eng. J.* **2023**, 471, 144578.

[12] J. Guo, M. Lu, X. Zhang, S. Sun, C. Han, Y. Zhang, X. Yang, S. V. Kershaw, W. Zheng, A. L. Rogach, *ACS Nano* **2023**, 17, 9290.

[13] J. Zhang, W. Shen, S. Chen, Z. Zhang, B. Cai, Y. Qiu, Y. Liu, J. Jiang, Y. He, M. Nan, *J. Phys. Chem. Lett.* **2023**, 14, 6639.

[14] H. Zhao, J. Xu, S. Zhou, Z. Li, B Zhang, X. Xia, X. Liu, S. Dai, J. Yao, *Adv. Funct. Mater.* **2019**, 29, 1808986.

[15] A. Jain, O. Voznyy, M. Korkusinski, P. Hawrylak, E. H. Sargent, *J. Phys. Chem. Lett.* **2017,** 8, 3179.

[16] Y. Wang, F. Yuan, Y. Dong, J. Li, A. Johnston, B. Chen, M. I. Saidaminov, C. Zhou, X. Zheng, Y. Hou, K. Bertens, H. Ebe, D. Ma, Z. Deng, S. Yuan, R. Chen, L. K. Sagar, J. Liu, J. Fan, P. Li, X. Li, Y. Gao, M. K. Fung, Z. Lu, O. M. Bakr, L. Liao, *Ange. Chem. Int. Ed.* **2021,** 60, 16164.

[17] E. J. Juarez-Perez, Z. Hawash, S. R. Raga, L. K. Ono, Y. Qi, *Energy Environ. Sci.* **2016,** 9, 3406.

[18] W. Zhou, F. Sui, G. Zhong, G. Cheng, M. Pan, C. Yang, S. Ruan, *J. Phys. Chem. Lett.* **2018,** 9, 4915.

[19] Y. Gao, C. S. S. Sandeep, J. M. Schins, A. J. Houtepen, L. D. A. Siebbeles, *Nat. Commun.* **2013,** 4, 2329.

[20] J. Hu, C. Bi, X. Zhang, B. Tian, Y. Lu, J. Tian, M. Sui, *Appl. Surf. Sci.* **2023,** 626,

157289.